Climate Dynamics
https://doi.org/10.1007/s00382-023-06744-4

Parameterizing the nonlinear feedback on ENSO from tropical instability waves (TIWs) by nonlinear eddy thermal diffusivity

Aoyun Xue[1,4] · Fei-Fei Jin[2] · Wenjun Zhang[1] · Julien Boucharel[2,3] · Jong-Seong Kug[4]

Received: 22 September 2022 / Accepted: 2 March 2023

Abstract
As the dominant form of mesoscale variability in the equatorial eastern Pacific, Tropical Instability Waves (TIWs) are known to interact with the El Niño and Southern Oscillation (ENSO) in complex ways. TIWs activity is modulated by the ENSO state and also provide significant feedback on ENSO via nonlinear dynamic heating (NDH), acting as a source of asymmetry between the El Niño and La Niña phases. In this work, we show that the interannual variability of TIWs-induced heat flux and NDH can be approximately expressed in terms of the mean meridional temperature gradient as TIWs tend to transport heat downgradient of the temperature anomalies along the Sea Surface Temperature (SST) front. The TIWs-induced NDH can be quantified as an asymmetric negative feedback on ENSO by a nonlinear thermal eddy diffusivity which depends on the background TIWs pattern and the ENSO-related linear and nonlinear processes. This proposed parameterization scheme can capture well the direct ENSO modulation on TIWs activity, the combination effect arising from the nonlinear interaction between ENSO and the cold tongue annual cycle, and associated ENSO nonlinearity. This parameterization scheme is effectively tested using four ocean reanalysis datasets with different horizontal resolutions that exhibit contrasted patterns of TIWs activity. This scheme may be useful for assessing the TIWs-induced feedback on ENSO in mechanistic ENSO models to better understand the dynamics of ENSO complexity.

Keywords TIWs · ENSO · TIWs-induced heat flux · Parameterization scheme

1 Introduction

Tropical Instability Waves (TIWs) are westward propagating long wave patterns of sea surface temperature (SST) that are commonly observed in the tropical Pacific and Atlantic Oceans, with a wavelength of 1000–2000 km and a period of 10–60 days (Legeckis 1977; Cox 1980; Weisberg and Weingartner 1988; Qiao and Weisberg 1995). TIWs partly arise from barotropic instability due to the strong shears between the equatorial zonal currents (Philander 1976, 1978; Yu et al. 1995), and to a greater extent from baroclinic instability induced by the strong meridional temperature gradient along the SST front in the eastern equatorial Pacific (EEP) (Hansen and Paul 1984; Wilson and Leetmaa 1988; Yu et al. 1995; Masina et al. 1999). Observational studies show that TIWs activity is modulated by both the EEP seasonal cycle and ENSO interannual variability due to the changes of SST background (e.g., Yu and Liu 2003; Im et al. 2012). For example, TIWs are active in boreal summer/autumn when the equatorial cold tongue is enhanced, while are suppressed in boreal spring when the cold tongue is strongly weakened

✉ Fei-Fei Jin
jff@hawaii.edu

✉ Wenjun Zhang
zhangwj@nuist.edu.cn

1 CIC-FEMD/ILCEC, Key Laboratory of Meteorological Disaster of Ministry of Education (KLME), Nanjing University of Information Science and Technology, Nanjing 210044, China

2 Department of Atmosphere Sciences, School of Ocean and Earth Science and Technology, University of Hawai'i at Manoa, Honolulu, HI 96822, USA

3 University of Toulouse, LEGOS, (CNRS, IRD, CNES, UPS), Toulouse, France

4 Division of Environmental Science and Engineering, Pohang University of Science and Technology (POSTECH), Pohang 37673, South Korea

Published online: 24 March 2023

(Hansen and Paul 1984; Pullen et al. 1987; Contreras 2002). TIWs activity is also strengthened (weakened) during the cold (warm) phase of ENSO due to the increased (decreased) meridional SST gradient (Vialard et al. 2001; Yu and Liu 2003; Wu and Bowman 2007; An 2008).

TIWs in turn have a substantial influence on ENSO and the tropical climate mean state through their induced nonlinear dynamical heating (NDH, i.e., the advection of ocean temperature by currents at the TIWs scale) (e.g., Jin et al. 2003; Jochum et al. 2007; Xue et al. 2020; Maillard et al. 2022), comparable to the one from atmospheric heat fluxes (Baturin and Niiler 1997; Xue et al. 2020, 2021). The interannual TIWs-induced NDH has been shown to act as an asymmetric negative feedback on ENSO, characterized by an anomalous cooling during El Niño and warming during La Niña (Bryden and Brady 1989; Swenson and Hansen 1999; Yu and Liu 2003; Menkes et al. 2006; An 2008; Imada and Kimoto 2012; Boucharel and Jin 2020; Xue et al. 2020). This feedback is stronger during La Niña than during El Niño which can partly contribute to ENSO amplitude asymmetry. However, most current ocean circulation models and reanalysis datasets still exhibit too coarse spatiotemporal resolutions to fully resolve TIWs mesoscale features, which hinders their ability to capture the TIWs-induced heat transport (Wang and McPhaden 1999; Graham 2014; Xue et al. 2020). Based on this fact, efficient quantification/parameterization could be a potential pathway to capture the TIWs rectification effects based on the slow-varying (seasonal mean) low-frequency information.

A simple statistical expression has been first proposed to describe the horizontal heat flux convergence due to TIWs based on the linear expression of SST anomaly over the Niño3.4 region (5°S–5°N, 170°–120°W) (An 2008). By incorporating this quantification into a simple ENSO Recharge Oscillator model (RO; Jin 1997), the TIWs-induced asymmetric heat transport was shown to partly explain the El Niño-La Niña amplitude asymmetry (An 2008; Xue et al. 2020). However, this simple quantification cannot well account for the seasonally modulated TIWs feedback on ENSO. Later, Imada and Kimoto (2012) developed a TIWs parameterization using the isopycnal-layer thickness diffusion coefficient into an atmosphere–ocean general circulation model, based on the original parameterization of mesoscale eddies along the baroclinic fronts at mid- or high-latitude (Gent and Mcwilliams 1990; Gent et al. 1995; Bryan et al. 1999). This parameterization, which employs an empirically-derived diffusion coefficient, represents well the baroclinic eddy heat transport due to TIWs supporting the significant influence of TIWs-induced heat transport on ENSO asymmetry but remains insufficient to reproduce the observed spatiotemporal characteristics of TIWs-induced NDH. Difficulties and uncertainties still exist in accurately parameterizing the complex spatiotemporal TIWs-induced heat effects on ENSO variability in these empirical expressions.

Recently, a stochastically forced linear model for TIWs amplitude with its damping rate modulated by the EEP annual cycle and ENSO has been introduced to describe the two-way nonlinear interactions between ENSO and TIWs (Boucharel and Jin 2020). This theoretical framework could successfully account for the nonlinear rectifications of TIWs activity on ENSO. Based on this model, we further proposed the formulation of seasonally dependent TIWs-induced heat flux and NDH using area-averaged (5°S–5°N, 90°–150°W) monthly mean SST anomaly (Niño3 index) in the EEP (Xue et al. 2020). However, this scheme accounts only for the temporal variability of TIWs-induced heat transport, and is not able to express its spatial characteristics. Therefore, improved quantification/parameterization of TIWs-induced heat flux in observations and ocean climate models remains to be developed to better reproduce the observed spatiotemporal TIWs-induced NDH.

In this work, we derive an effective parameterization scheme of spatiotemporal TIWs-induced heat flux and NDH based on our established framework of ENSO-TIWs interaction (Boucharel and Jin 2020; Xue et al. 2020). This new scheme aims to capture the observed TIWs-induced NDH feedback on ENSO spatial and temporal variability accurately, which would be incorporated in theoretical and intermediate complexity models to improve ENSO simulations and predictions. The remainder of the paper is organized as follows. Section 2 presents the datasets, methods and definition of complex spatiotemporal TIWs indices. In Sect. 3, we propose a new parameterization scheme of spatiotemporal TIWs-induced heat transport based on the TIWs stochastic forced linear model. Section 4 verifies the performance of the parameterization scheme through comparison with the traditional band-pass filtering method. In Sect. 5, we test the effectiveness and general applicability of the parameterization scheme in different reanalysis datasets with contrasted horizontal resolutions. Section 6 summarizes our results and discusses some unsettled questions for future work.

2 Data and methodology

2.1 Ocean reanalysis products

We utilize the oceanic potential temperature and currents datasets from four oceanic reanalysis products: (1) the National Center for Environmental Predictions (NCEP) Global Ocean Data Assimilation System (GODAS) pentad product at a $1/3° \times 1°$ horizontal resolution from 1980 to 2018 (Behringer and Xue 2004; Saha et al. 2006); (2) the Hybrid Coordinate Ocean Model (HYCOM) daily reanalysis product with horizontal resolution at $0.08° \times 0.08°$ from

1994 to 2015 (Chassignet et al. 2007); (3) the GLORYS12 daily reanalysis product which is produced and distributed by Copernicus Marine Environment Monitoring Service (CMEMS) at a 0.083° × 0.083° horizontal resolution from 1993 to 2019 (Lellouche et al. 2021); (4) the Cube92 model products of Estimating the Circulation and Climate of the Ocean, phase II (ECCO2) with a horizontal resolution at 1/4° × 1/4° from 1992 to 2019 (Menemenlis et al. 2008). The construction of the parameterization scheme is based on the HYCOM dataset (Sect. 3–4) and the other three datasets are used for testing its effectiveness (Sect. 5). The statistical significances are determined based on a two-tailed Student's *t* test.

2.2 TIWs-induced heat flux and NDH measurement

The effectiveness of the proposed parameterization scheme is verified through comparison with the results from traditional band-pass filtering method in the four reanalysis datasets. Conventionally, each variable X can be separated into a mean climate state (overbar), low-frequency component (over 60-day; tilde) and eddy component (less 60-day; prime) and therefore X can be expressed as $X = \overline{X} + \widetilde{X} + X'$ (Lyman et al. 2005; Xue et al. 2020, 2021). As TIWs have a broad spectral peak in the 10–60-day range, we apply a 10–60-day band-pass Fourier filtering method to the ocean temperature and current fields within the mixed layer (0-50 m) to extract TIWs signals (Qiao and Weisberg 1995, 1998; Lyman et al. 2005; Shinoda et al. 2009; Wang et al. 2020). The eddy component at 10–60-day timescales usually encompasses both TIWs and a small portion of the intraseasonal Kelvin waves. The contributions of the intraseasonal Kelvin waves on heat budget in the EEP can be ignored, since the TIWs stand out as the dominant signal (Menkes et al. 2006; Graham 2014). The TIWs-induced heat flux is estimated from the nonlinear rectified effect of anomalous temperature transport by anomalous currents at the intraseasonal timescales, which can be written as:

$$\overrightarrow{HF_{TIW}} = -\widetilde{\overrightarrow{V'T'}} = \left(\widetilde{-u'T'}\right)\vec{i} + \left(\widetilde{-v'T'}\right)\vec{j} + \left(\widetilde{-w'T'}\right)\vec{k}, \quad (1)$$

where T' and (u', v', w') represent the oceanic mixed-layer anomalies of temperature and ocean currents at the TIWs timescales (10–60-day). The tilde denotes a three-month running mean to highlight the low-frequency variability. As the divergence of the eddy heat flux, TIWs-induced NDH act as a dynamical heating source for ocean temperatures, which could be referred to as the TIWs' rectification effect onto the ENSO heat budget. The effect of TIWs on the heat budget on seasonal time scales can be expressed as:

$$NDH_{TIW} = \nabla \cdot \overrightarrow{HF_{TIW}} = \left(-\frac{\partial \widetilde{u'T'}}{\partial x}\right) + \left(-\frac{\partial \widetilde{v'T'}}{\partial y}\right) + \left(-\frac{\partial \widetilde{w'T'}}{\partial z}\right). \quad (2)$$

TIWs mainly tend to transport warm water from the Intertropical Convergence Zone (ITCZ) to the equatorial cold tongue (downgradient of the temperature anomalies along the SST front). Previous studies have shown that the TIW-induced zonal and vertical heat flux components onto the mean climate state and ENSO variability are negligible within the mixed layer (Hansen and Paul 1984; Bryden and Brady 1989; Menkes et al. 2006; Xue et al. 2020). Therefore, the TIWs-induced heat flux (HF_{TIW}) and associated NDH (NDH_{TIW}) within the mixed layer could be largely represented by the meridional components:

$$\begin{aligned} \overrightarrow{HF_{TIW}} &= \left(\widetilde{-\overrightarrow{V'T'}}\right) = \left(\widetilde{-v'T'}\right)\vec{j} \\ NDH_{TIW} &= \nabla \cdot \overrightarrow{HF_{TIW}} = \left(-\frac{\partial \widetilde{v'T'}}{\partial y}\right) \end{aligned}. \quad (3)$$

As shown by the time-averaged TIWs-induced heat flux and NDH calculated in the EEP using the high resolution HYCOM dataset, most of the eddy heat transport occurs within the mixed layer (0-50 m) along the SST front (~ 3°N) where TIWs are most active (Fig. 1a). As the divergence of the eddy heat flux, TIWs-induced NDH occurs near the equator (2°S–4°N) (Fig. 1b), which contributes to the ENSO development. As shown in Fig. 1c, d, both the eddy heat flux and NDH due to TIWs in EEP nearly exhibit a uniform behavior in the vertical distribution. So, we could assume the related parameters in our parameterization scheme (Sect. 3) to be constants in depth as a reasonable approximation.

2.3 Definition of TIWs spatiotemporal indices

A complex TIWs index has been proposed to characterize the temporal variations of TIWs activity in our earlier studies (Boucharel and Jin 2020; Xue et al. 2020, 2021). Here, we extend the complex temporal (one-dimensional) TIWs index to three-dimensional TIWs index to account for the spatiotemporal variability of TIWs activity. Utilizing TIWs spatiotemporal coherency, we use a simple set of base points in zonal direction, equally spaced according to the typical TIWs wavelength, to formulate the spatiotemporal complex index of TIWs activity. Hence, the spatiotemporal TIWs values at each grid point (t, *x*, *y*) could be represented by four adjacent fixed points. The real/imaginary part of the complex TIWs index (*TIW1/TIW2*) is simply extracted as the equally spaced and weighted (but with alternating signs) summation of unfiltered surface meridional current anomalies (v'), which could be written as:

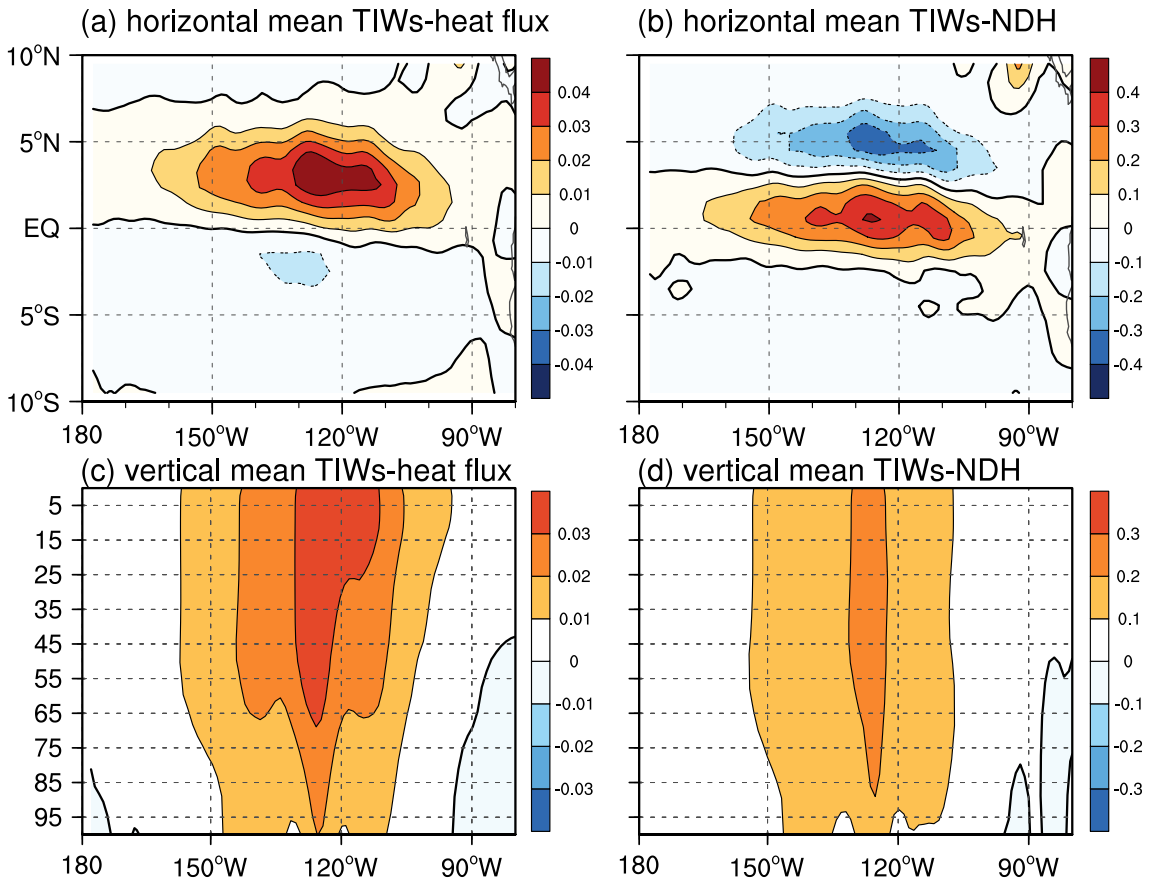

Fig. 1 **a**, **b** Horizontal distributions of mean TIWs-induced heat flux (m°Cs^{-1}) and NDH (°Cmonth^{-1}) within the mixed layer (0–50 m), respectively; **c**, **d** Vertical distributions of mean TIWs-induced heat flux (averaged between 0 and 6°N) and NDH (averaged between 2°S and 4°N), respectively

$$TIW1(t,x,y) = \frac{v'(t,x-l,y)-v'\left(t,x-\frac{l}{2},y\right)+v'\left(t,x+\frac{l}{2},y\right)-v'(t,x+l,y)}{4}$$
$$TIW2(t,x,y) = \frac{v'\left(t,x-\frac{5l}{4},y\right)-v'\left(t,x-\frac{3l}{4},y\right)+v'\left(t,x+\frac{l}{4},y\right)-v'\left(t,x+\frac{3l}{4},y\right)}{4}, \quad (4)$$

where l represents the wavelength (in degrees) determined from the leading complex empirical orthogonal function (CEOF) mode (Xue et al. 2020, 2021). There is a 90° zonal phase shift (also $\frac{l}{4}$) between the real (TIW1) and imaginary (TIW2) part of the complex TIWs index ($Z = TIW1 + iTIW2$). It should be noted that the results are not sensitive to the number (such as 4, 6 or 8) of base points chosen. The spatiotemporal TIWs amplitude is then expressed as:

$$|Z|^2(t,x,y) = TIW1(t,x,y)^2 + TIW2(t,x,y)^2 \quad (5)$$

To examine the effectiveness of the complex TIWs index in capturing the TIWs spatial features, we compare the newly-defined TIWs amplitude with traditional definition of TIWs intensity, which is often measured by the variance (i.e., square) of band-pass filtered SST or current anomalies. As shown in Fig. 2a, the mean TIWs amplitude derived from our new method highly resembles that from the traditional 10–60-day band-pass filtering method, confirming the effectiveness of the three-dimensional complex TIWs indices. Similarly, the time series of domain (0°–6°N, 110°–150°W) averaged TIWs amplitude derived from these two methods are highly correlated ($R = 0.95$) (Fig. 2b). Note that the complex spatiotemporal TIWs index presented here doesn't require band-pass filtering preprocessing of the long-term raw datasets and could therefore serve as an effective and concise index for real-time monitoring of spatiotemporal TIWs activity.

3 Parameterization scheme of TIWs-induced heat transport

As discussed in the introduction, a stochastically forced linear model for TIWs amplitude which is modulated by the EEP annual cycle and ENSO has been introduced recently (Boucharel and Jin 2020) and can be written as:

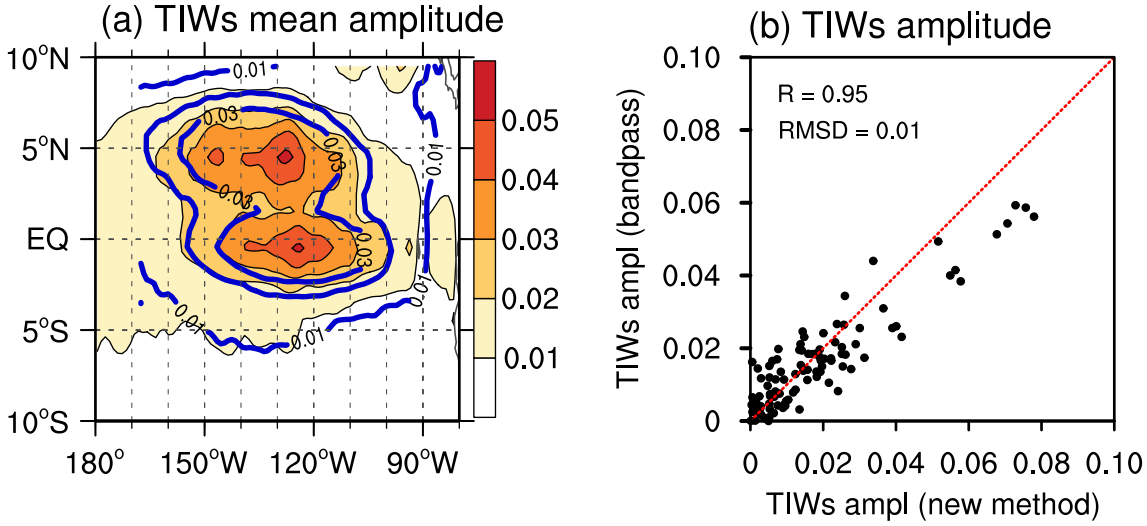

Fig. 2 **a** Mean states of TIWs variance calculated as the 10–60-day band-pass filtered meridional velocity anomalies (v') (shadings, m^2s^{-2}) and TIWs amplitude derived from the new method presented in Sect. 2.3 (contours, m^2s^{-2}); **b** Scatterplot of the relationship between monthly TIWs amplitudes averaged over TIWs active region (0–6°N, 110–150°W) from the two calculation methods. Correlations and root mean square deviation are included in the top left corner

$$\frac{dZ}{dt} = \left[-\left(\gamma_0 + \frac{2i\pi}{T}\right) + \left(\gamma_A \cos\frac{2\pi(t-\varphi)}{T_A}\right) + \left(\gamma_N Niño3(t)\right)\right] Z + \omega(t), \tag{6}$$

where Z denotes the complex TIWs index, dZ/dt is the TIWs tendency, $\frac{2i\pi}{T}$ the TIWs oscillator with a period $T = 36$ days, $\cos\frac{2\pi(t-\varphi)}{T_A}$ the annual forcing with a period $T_A = 365$ days and φ the phase for the annual damping rate which is identified as 120 days, so that the TIWs amplitude reaches a maximum in boreal summer/autumn and a minimum in spring. *Niño3* is the ENSO forcing (averaged SST anomaly in the domain of 5°S–5°N, 90°–150°W) and $\omega(t)$ is the white noise forcing. γ_0 is the mean damping rate, and γ_A and γ_N are the annual and interannual modulation of TIWs damping rate by the EEP annual cycle and ENSO, respectively. Since $T << T_A$ and $T << Ni\tilde{n}o3$ period, previous study has showed that the low-frequency TIWs amplitude can be formulated as the second-order approximation of the simple TIWs model's analytical solution (Boucharel and Jin 2020). Considering that TIWs-induced heat flux is largely proportional to the TIWs amplitude (Xue et al. 2020; Boucharel and Jin 2020), the parameterization scheme of TIWs-induced heating effects on ENSO could be well formulated by the analytical solution of TIWs amplitude. Through a proper simplification with neglecting the high-order terms, the temporal TIWs-induced heat flux can be written as follows:

$$HF_{TIW}(t) \approx \lambda\left(\frac{\gamma_N}{\gamma_0} Niño3(t) + 2\frac{\gamma_A\gamma_N}{\gamma_0^2}\cos\left(\frac{2\pi(t-\varphi)}{T_A}\right) \times Niño3(t) + \left(\frac{\gamma_N}{\gamma_0}\right)^2 Niño3(t)^2\right), \tag{7}$$

where λ is a constant, representing the mean state of TIWs variance (i.e., amplitude) and the expression between bracket is the interannual modulations of TIWs amplitude's 2nd order analytical solution (Boucharel and Jin 2020). However, this formulation could not account for the spatial variations of TIWs-induced heat flux since it is only considering temporal variations. A three-dimensional formulation of TIWs-induced heat flux and NDH should be further proposed to better account for the TIWs contribution to ENSO spatiotemporal characteristics.

Considering the remarkably linear relationship between the TIWs-induced heat flux and TIWs amplitude, we propose the spatiotemporal (i.e., three-dimensional) TIWs amplitude (Sect. 2.3) to capture the TIWs-induced heating effects. As shown in Fig. 3, the newly-defined TIWs amplitude is highly correlated with area-averaged TIWs-induced heat flux and NDH based on the HYCOM dataset (Eq. 3). Therefore, the TIWs-induced heat flux and NDH at each grid point in the EEP could be theoretically expressed using the analytical TIWs amplitude in consideration of the proportionality. Accordingly, we can extend the temporal (one-dimensional) parameterization scheme (Eq. 6)

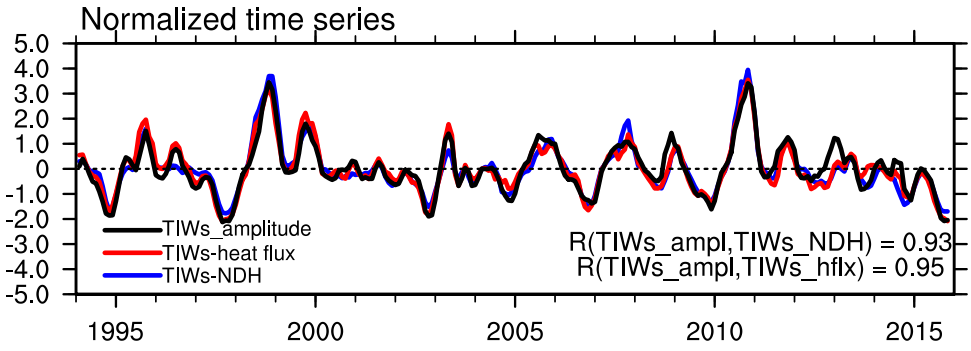

Fig. 3 Interannual parts of the normalized time series of area-averaged TIWs amplitude (black line, m^2s^{-2}), TIWs-induced heat flux (red line, $m°Cs^{-1}$) over the TIWs active region (0–6°N, 110–150°W) and NDH (blue line, $°Cmonth^{-1}$) (2°S–4°N, 110–150°W), respectively

of interannual TIWs-induced heat flux to account for the spatiotemporal (three-dimension) variability as:

$$-\widetilde{v'T'}(t,x,y) \approx \lambda(x,y)\left(\begin{array}{l} K_0(x,y)Niño3(t,x,y) + K_1(x,y)\cos\left(\dfrac{2\pi(t-\varphi)}{T_A}\right) \\ \times Niño3(t,x,y) + K_2(x,y)Niño3(t,x,y)^2 \end{array}\right). \tag{8}$$

Here, T' and v' represent the mixed-layer averaged intraseasonal (10–60-day) anomalies of temperature and meridional ocean currents, respectively. Similarly, $\lambda(x,y)$ represents the horizontal mean state of TIWs variance and determines the spatial distribution of TIWs-induced heat flux. The corresponding spatial coefficients $K_0(x,y)$, $K_1(x,y)$ and $K_2(x,y)$ represent the relative contributions to the total TIWs heat transport from three main governing terms: the direct linear ENSO forcing, the combination effect emerging from deterministic nonlinear interactions between ENSO and the cold tongue annual cycle, and ENSO high order nonlinearity (Stuecker et al. 2013, 2015; Xue et al. 2020; Boucharel and Jin 2020). Here, the combination effect explains the seasonal dependence of ENSO modulation on TIWs activity, different from the direct ENSO impact. The ENSO high order nonlinearity accounts for the asymmetry of TIWs-induced thermal effect between the ENSO warm and cold phase.

Although TIWs activity could be regarded as a random process at seasonal to interannual scale, TIWs could lead to large-scale heat transport and redistribution in the EEP through nonlinear rectification effect. TIWs can transport warm water from the northern ITCZ to the equator in EEP by relentless stirring of water and lead to the eddy-induced heat fluxes and associated NDH. Acting in a manner analogous to molecular thermal diffusivity, TIWs-induced heat flux would be therefore proportional to the local slowly-varying meridional temperature gradient and then could be theoretically expressed in terms of the monthly temperature gradient as:

$$-\widetilde{v'T'} = -K\left(\frac{\partial\tilde{T}}{\partial y}\right), \tag{9}$$

where $\frac{\partial\tilde{T}}{\partial y}$ represents the monthly meridional temperature gradient along the SST front and the above tilde refers to a three-month running average. $\boldsymbol{K}\left(m^2s^{-1}\right)$ is the coefficient of eddy thermal diffusion, which is an important parameter indicative of the eddy heat transfer rate. The larger the diffusion coefficient, the higher the TIWs heat exchange efficiency. This closure scheme is often referred to as the Flux-Gradient theory. Motivated by the mechanistic TIWs-induced heat flux expression in Eq. 8 and the fact TIWs transport heat down the slow-varying meridional ocean temperature gradient, we propose a heuristic form for the three-dimensional TIWs-induced heat flux as follows:

$$-\widetilde{v'T'}(t,x,y) = \lambda(x,y)\frac{\partial\tilde{T}}{\partial y}(t,x,y)\left(K_0(x,y) + K_1(x,y)\cos\left(\frac{2\pi(t-\varphi}{T_A}\right) + K_2(x,y)Niño3(t)\right), \tag{10}$$

in which the eddy diffusion coefficient K in the scheme is expressed as:

$$\boldsymbol{K} = \lambda(x,y)\left(\begin{array}{ccc} K_0(x,y) & K_1(x,y) & K_2(x,y) \end{array}\right)\left(\begin{array}{c} 1 \\ \cos\left(\frac{2\pi(t-\varphi}{T_A}\right) \\ Niño3(t) \end{array}\right). \tag{11}$$

As the units and dimensions on both sides of the parameterization scheme have to be identical (Table. 1), the mean state of TIWs variance λ should be measured with

Table 1 Units and characteristic scales of variables in the parameterization scheme of TIWs-induced heat flux

Variables	TIWs-induced heat flux ($-\widetilde{v'T'}$)	TIWs mean variance (λ)	Meridional SST gradient $\left(\frac{\partial \tilde{T}}{\partial y}\right)$	Parameters (K_0, K_1, K_2)
Units	$m°Cs^{-1}$	m^2s^{-2}	$°Cm^{-1}$	s
Characteristic scales	$\frac{L\theta}{T}(10^{-2})$	$\frac{L^2}{T^2}(10^{-2})$	$\frac{\theta}{L}(10^{-6})$	$T(10^6)$

the meridional component of velocity (v') at the TIWs scale (Fig. 2a). Correspondingly, $\lambda(x, y)$ is measured as:

$$\lambda(x, y) = \overline{v'^2}(x, y). \tag{12}$$

We then estimate the three key parameters $K_0(x, y)$,$K_1(x, y)$ and $K_2(x, y)$ from the high-resolution HYCOM dataset through a multiple linear regression analysis. As shown in Fig. 4, all the spatial distributions of all three parameters show roughly uniform spatial structures over the TIWs active region (0°–6°N, 110°–150°W). Despite that the three parameters exhibit some spatial differences, the results by using the two-dimensional K patterns ($K_0(x, y)$, $K_1(x, y)$ and $K_2(x, y)$) in the new scheme are largely consistent with those based on the constant K (not shown). Therefore, to keep the proposed parameterization scheme as succinct and effective as possible, we assume these three state-dependent parameters K_0, K_1 and K_2 are constants in space. These three parameters are approximated as a domain average ($K_0 = -0.6 \times 10^6 s$,$K_1 = -0.2 \times 10^6 s$ and $K_2 = 0.1 \times 10^6 s$), which are consistent with estimates from the TIWs stochastic model $\left(\frac{\gamma_N}{\gamma_0}, 2\frac{\gamma_A\gamma_N}{\gamma_0^2}\right.$ and $\left.\left(\frac{\gamma_N}{\gamma_0}\right)^2\right)$ (Boucharel and Jin 2020; Xue et al. 2020). The parameterization scheme of horizontal TIWs-induced heat flux can be simplified as:

$$-\widetilde{v'T'}(t, x, y) = \overline{v'^2}(x, y)\frac{\partial \tilde{T}}{\partial y}(t, x, y)\left\{K_0 + K_1 \cos\left(\frac{2\pi(t-\varphi)}{T_A}\right) + K_2 Niño3(t)\right\} \tag{13}$$

As the convergence of TIWs-induced heat flux, TIWs-induced NDH serves as a dynamic heating source for ENSO-related SST and could be formulated as the partial derivative of heat flux in the meridional direction:

$$NDH_{TIW}(t, x, y) = -\frac{\partial \widetilde{v'T'}}{\partial y} = \frac{\partial\left[\overline{v'^2}(x, y)\frac{\partial \tilde{T}}{\partial y}(t, x, y)\left\{K_0 + K_1 \cos\left(\frac{2\pi(t-\varphi}{T_A}\right) + K_2 Niño3(t)\right\}\right]}{\partial y}. \tag{14}$$

One can assess TIWs-induced heat feedback on ENSO by extracting information from the slowly-varying SST gradient and ENSO SST variability, since the mean TIWs variance and related parameters have been determined as constants at each grid point. Compared to the traditional method, this new scheme with no need for bandpass filtering to extract the high-frequency TIWs, can realistically represent TIWs-induced heat effect on ENSO. In this case, this scheme can be easily applied online in theoretical and intermediate complexity ENSO models to study the effect of TIWs on ENSO characteristics. However, how well the observed TIWs-induced heat transport could be represented by the parameterization scheme still needs to be addressed. In the following section, we will test the performance of the proposed TIWs-induced heat transport quantification.

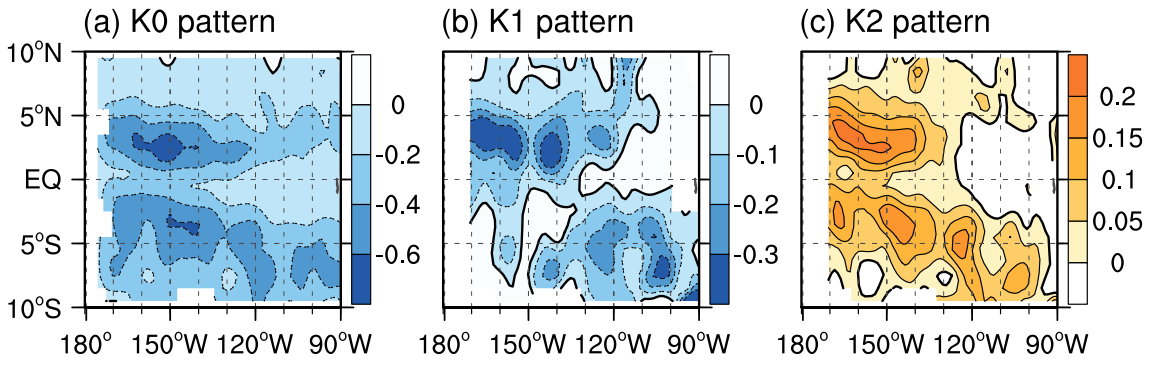

Fig. 4 Spatial patterns of K_0, K_1 and K_2 (units: 10^6 s^{-1}) in Eq. (10) inferred from a multiple linear regression method using high-resolution HYCOM dataset

4 Performance of the TIWs parameterization scheme

To evaluate the performance of the TIWs-induced heat transport parameterization scheme, we conduct an EOF analysis of the monthly TIWs-induced heat fluxes over the EEP region (10°S–10°N, 180°–90°W) using the high-resolution HYCOM dataset. Here the traditional estimate of TIWs-induced heat flux and NDH are calculated from 10 to 60-day band-pass filtered temperature (T') and meridional velocity (v') (Eq. 3) and the newly-proposed parameterization scheme refers to our proposed formulations (Eqs. 13 and 14). The leading EOF modes of TIWs-induced heat flux calculated from the two methods, respectively, account for 35% and 45% of the total variances, and are well separated from the corresponding second modes as per the criterion of North et al. (1982). The spatial patterns of two principal modes give a good account of the equatorward heat flux convergence (Fig. 5a, b) and the corresponding leading PC time series (PC1) are highly correlated ($R = 0.88$) (Fig. 5c). It suggests that our parameterization scheme reproduce well both the spatial and temporal features of the TIWs-induced heat flux and NDH. We also show in Fig. 6 the interannual variation of TIWs-induced heat flux (0°–6°N, 150°–110°W) and NDH (2°S–4°N, 150°–110°W) after applying a domain average. Their high consistence again confirms the ability of the parameterization scheme in capturing TIWs-induced heating effects.

To investigate the consistency in terms of the dominant physical processes, we conduct a spectral analysis of the TIWs-induced heat flux and NDH inferred from the two methods (Fig. 7). Our scheme exhibits almost same spectral structure as the traditional band-pass filtering method, especially around three peaks near 0.33 yr^{-1} (~ 36-month), 0.67 yr^{-1} (~ 18-month), and 1.33 yr^{-1} (~ 9-month). The 0.33 yr^{-1} largely represents the ENSO frequency (f), indicating the direct ENSO modulation on the TIWs activity. The 0.67 yr^{-1} and 1.33 yr^{-1} mathematically equal to $1 \pm f$ (1 being the annual cycle frequency), reflecting the combination effect on the TIWs activity from the nonlinear interaction between the ENSO and the EEP annual cycle (Stuecker et al. 2013, 2015; Xue et al. 2020; Boucharel and Jin 2020). The combination effect largely captures

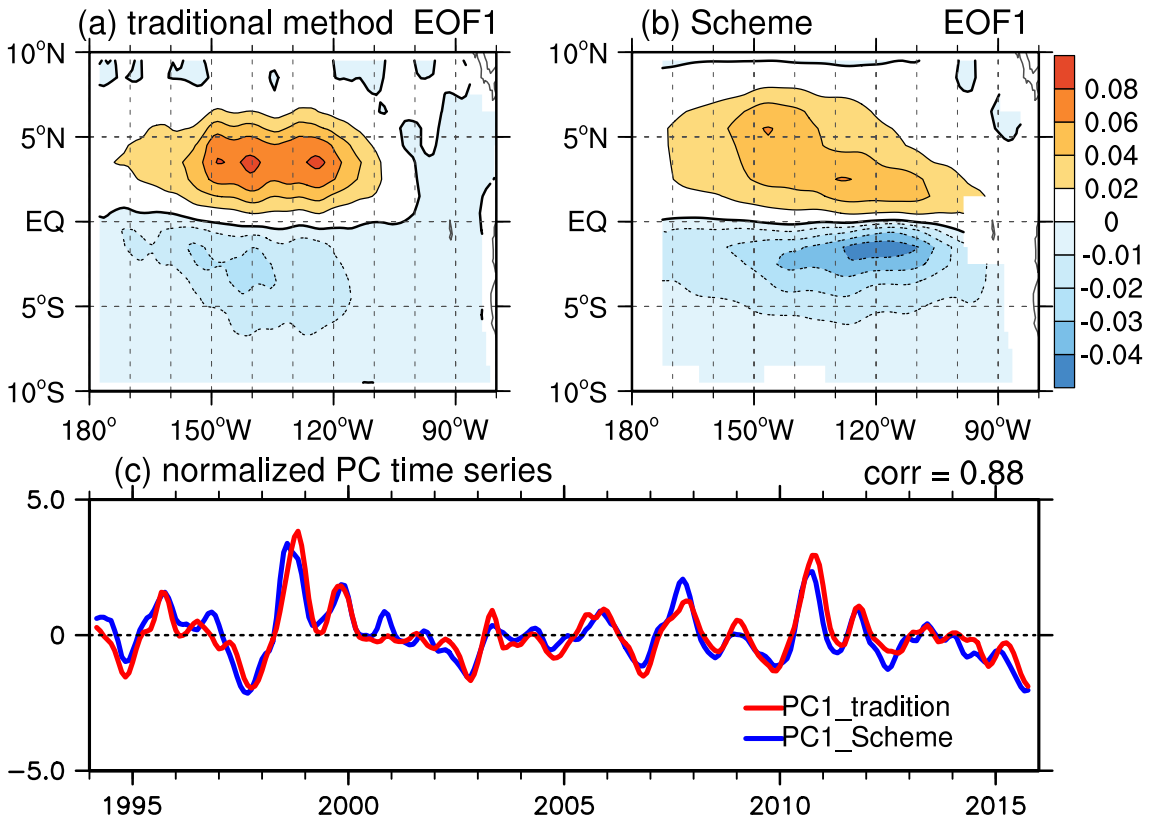

Fig. 5 Spatial patterns of the leading EOF modes of the traditional (**a**) and parameterized (**b**) TIWs-induced heat flux (units: m°Cs^{-1}) over the EEP region (10°S–10°N, 180°–80°W) derived from the high-resolution HYCOM dataset; **c** Corresponding normalized Principal Components (PC) time series of the traditional (red line) and parameterized (blue line) TIWs-induced heat flux leading EOF modes. Correlations are statistically significant above the 99% confidence level

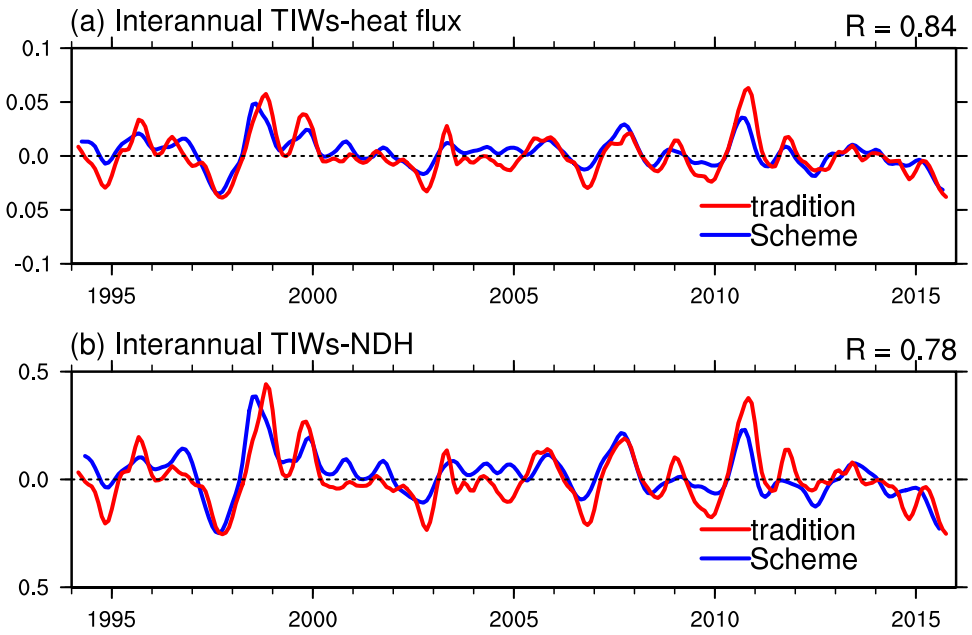

Fig. 6 **a** Three-month running mean and area averaged traditional (red lines) and parameterized (blue lines) interannual TIW-induced heat flux (0–6°N, 110–150°W) and **b** NDH (2°S–4°N, 110–150°W) time series within the mixed layer (0–50 m) from HYCOM dataset. Correlations are included in the top right corner of each panel and statistically significant above the 99% confidence level

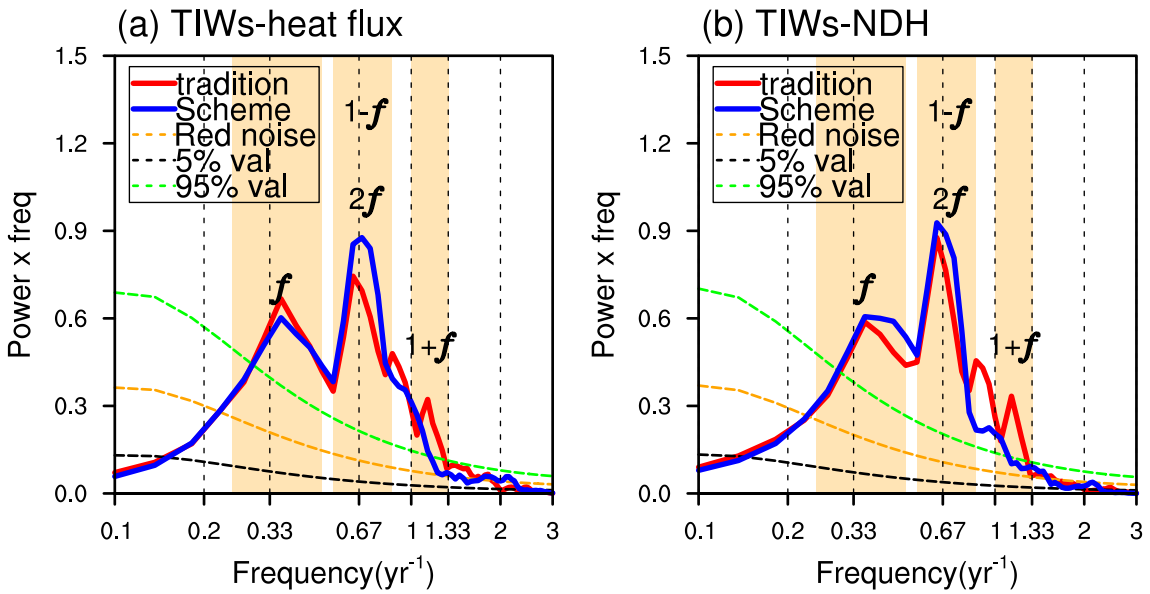

Fig. 7 (a, b) Fast Fourier transform (FFT) power spectra of the normalized monthly TIWs-induced heat flux (units: m°Cs^{-1}) and NDH (units: °Cmonth^{-1}). Red lines are for the traditional band-pass filtering method and blue lines for the parameterization scheme. The plotting format forces the area under the power curve to be equal in any frequency band to the variance. The dashed orange lines are the red-noise spectrum inferred from first order auto-regressive process. The 5% (95%) confidence intervals are shown by the dashed black (green) lines

the seasonally modulated ENSO effect on TIWs activity. We note that the modulation on TIWs activity by ENSO high order nonlinearity at frequency 2 f (~0.66 yr^{-1}) falls within the band of frequency $1-f$, which also contributes to this spectral peak. Different from traditional empirical data-driven quantification methods, our proposed parameterization scheme provides a clear picture of the physical mechanisms responsible for the TIWs-induced thermal feedback on ENSO.

We next compare the TIWs-induced heat flux and NDH during the peak phase (October to December, OND) of El Niño and La Niña events to investigate the TIWs thermal feedback during the ENSO mature phase. The ENSO events are identified according to the definition

by the Climate Prediction Center based on the oceanic Niño index averaged over the Niño 3.4 region (5°S–5°N, 120°–170°W) (Table 2). Despite the existence of biases in the magnitudes and spatial distributions (Fig. 8) potentially originating from the assumption of the three parameters K_0,K_1 and K_2 being constants in space (Fig. 0.4), the composited eddy heat flux and NDH are rather realistically reproduced by our scheme and approximately consistent with those inferred from the traditional band-pass filtering method. Some neglected processes, such as the barotropic energy conversion due to zonal current shear (e.g., Philander 1976, 1978; Yu et al. 1995), the ENSO higher order nonlinearity processes (e.g., Xue et al. 2020) and sub-mesoscale oceanic eddy processes (e.g., Wang et al. 2022), might also lead to the spatiotemporal differences of TIW-induced heat flux. Nevertheless, our parameterization scheme can effectively capture the TIWs-induced asymmetric feedback on ENSO (An 2008; Imada and Kimoto 2012), with values of up to 0.4 °C/month over the EEP during La Niña and nearly − 0.2 °C/month during El Niño.

To further test the performance of our parameterization scheme in capturing TIWs' contributions to ENSO development, we also asses TIWs' contributions to the ENSO growth rate (Jin et al. 2006; Kim and Jin 2011; Wengel et al. 2021). TIWs-induced NDH can be decomposed into three parts to examine the relative contributions of the three terms in Eq. 14 on ENSO growth:

$$
\begin{aligned}
Q_1 &= -\frac{\partial}{\partial y}\left(\overline{v'^2}(x,y)\frac{\partial \tilde{T}}{\partial y}K_0\right)\\
Q_2 &= -\frac{\partial}{\partial y}\left(\overline{v'^2}(x,y)\frac{\partial \tilde{T}}{\partial y}K_1\cos\left(\frac{2\pi(t-\varphi}{T_A}\right)\right)\\
Q_3 &= -\frac{\partial}{\partial y}\left(\overline{v'^2}(x,y)\frac{\partial \tilde{T}}{\partial y}K_2 Niño3(t)\right).
\end{aligned}
\tag{15}
$$

Q_1 is the linear ENSO term, Q_2 the combination effect term and Q_3 the ENSO high-order nonlinearity term. By

Table 2 Classification of ENSO events during the 1994–2016 period

El Niño years	La Niña years
1994/95, 1997/98, 2002/03, 2004/05, 2006/09, 2009/10, 2015/16	1995/96, 1998/99, 1999/00, 2000/01, 2005/06, 2007/08, 2008/09, 2010/11, 2011/12

ENSO events are identified based on a threshold of 0.5 standard deviations of the DJF Niño3.4 index. ENSO years are labeled year(0)/year(1), where 0 and 1 refer to the ENSO developing and decaying year, respectively

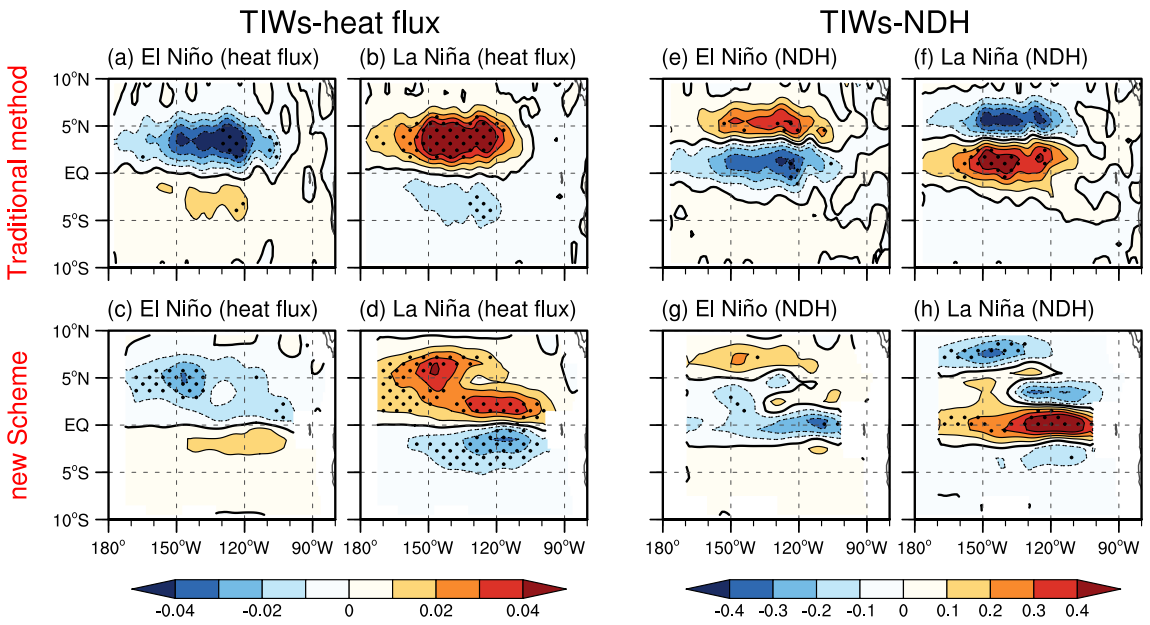

Fig. 8 Composite patterns of TIWs-induced heat flux (units: m°Cs^{-1}) within the mixed layer (0–50 m) during the peak phase (OND) of the El Niño (**a**) and La Niña (**b**) events from traditional band-pass filtering method; **c**, **d** same in (**a**, **b**) but for the parameterized TIWs-induced heat flux with the new scheme. Black dots denote statistically significance at the 99% confidence level using two-tailed Student's *t* test. **e**–**h** Same as (**a**–**d**) but for the TIWs-induced NDH (units: °Cmonth^{-1})

performing a linear regression of TIWs-induced NDH onto Niño3.4 index from July to December of all years, we can approximately derive the relative contributions on ENSO growth rate (GW) as:

$$
\begin{aligned}
GW_{TIWs} &= GW_1 + GW_2 + GW_3 \\
GW_1 &= \frac{Q_1}{\tilde{T}} = \frac{Q_1}{Niño34(t)}(ENSO) \\
GW_2 &= \frac{Q_2}{\tilde{T}} = \frac{Q_2}{Niño34(t)}(C\_effect) \\
GW_3 &= \frac{Q_3}{\tilde{T}} = \frac{Q_3}{Niño34(t)}\left(ENSO^2\right)
\end{aligned}
\tag{16}
$$

where the bracket "<>" denotes a domain average over the Niño3.4 region. As shown in Fig. 9a, the TIWs contributions to ENSO development calculated based on our scheme agree well with the estimates from the traditional method for all three quantified terms. The ENSO direct contribution (GW_1) acts as strongly negative feedback onto ENSO growth, whereas the term related to ENSO high order nonlinearity (GW_3) acts as positive feedback. The contribution of the combination effect term (GW_2) is negligible since the seasonality is weak during the ENSO developing phase (July–December). Overall, TIWs activity acts as a net negative feedback (GW_{TIWs}) on ENSO growth. When we break down the ENSO events into El Niño and La Niña events (Fig. 9b, e), the contributions of TIWs nonlinear terms (GW_3) to ENSO are opposite in sign with asymmetric amplitude, showing strong positive feedback during El Niño and relatively weak negative feedback during La Niña. It corresponds well to the observation that TIWs activity is strongly strengthened during La Niña events and weakly suppressed during El Niño events (An 2008; Xue et al. 2020; Wengel et al. 2021). When warm SST anomalies of the cold tongue reach a threshold value, TIWs activity is completely suppressed and lead to a TIWs-free condition. In contrast, a further drop of the cold SST anomalies in the EEP could lead to a more unstable baroclinicity by increasing the SST gradient and therefore to a faster TIWs growth. This physical process of the asymmetric feature of TIWs-induced NDH is well expressed in our parameterization scheme.

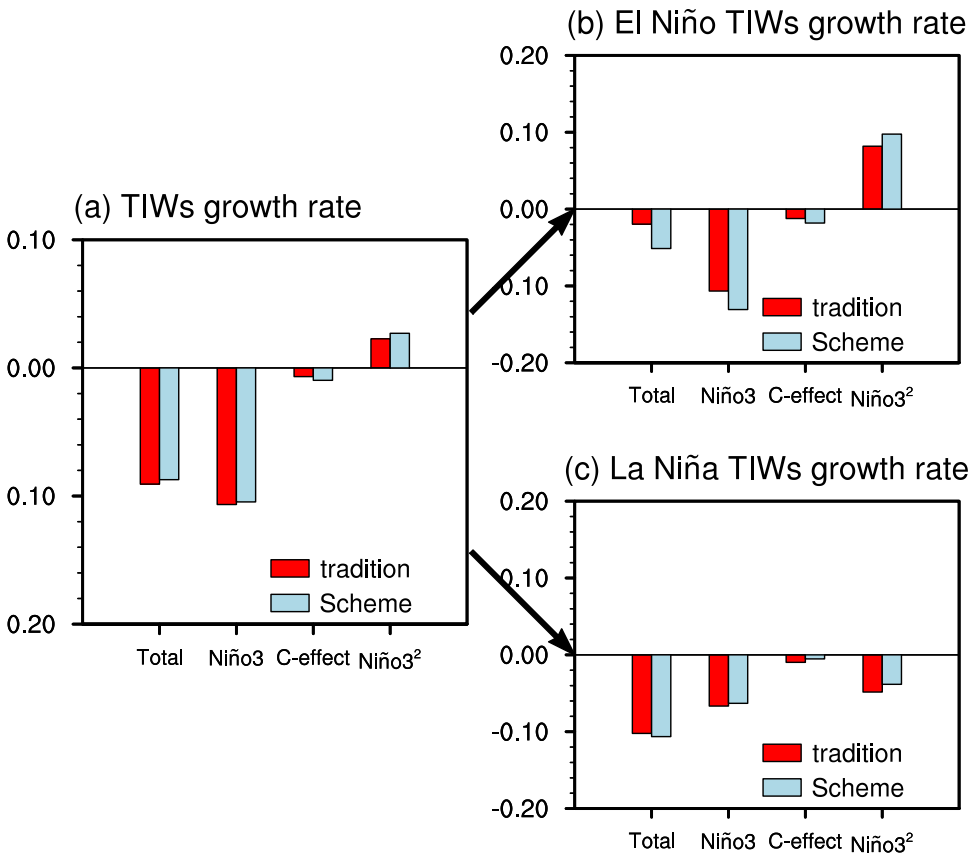

Fig. 9 **a** The traditional (red) and parameterized (blue) TIWs-induced NDH contributions to ENSO growth rate (GW) (units: month^{-1}). The bars, from left to right, indicate the total contributions of TIWs, linear ENSO (Niño3) term, the combination effect (C-effect) term and ENSO high-order nonlinearity (Niño3^2) term; **b**, **c** Same as (**a**) but for El Niño and La Niña mature phase respectively. All contribution coefficients are statistically significant above the 99% confidence level

5 Sensitivity to different horizontal resolutions of datasets

At present, TIWs are still not well resolved in most current climate models and reanalysis datasets due to the coarse resolutions and unrealistic physical processes (Huang et al. 2010; Graham 2014). The different horizontal resolutions of oceanic datasets are therefore expected to lead to different values of the inferred key parameters and of TIWs mean variance in the parameterization scheme (Eq. 14). We now examine the sensitivity of the TIWs performance and the three estimated parameters to the horizontal

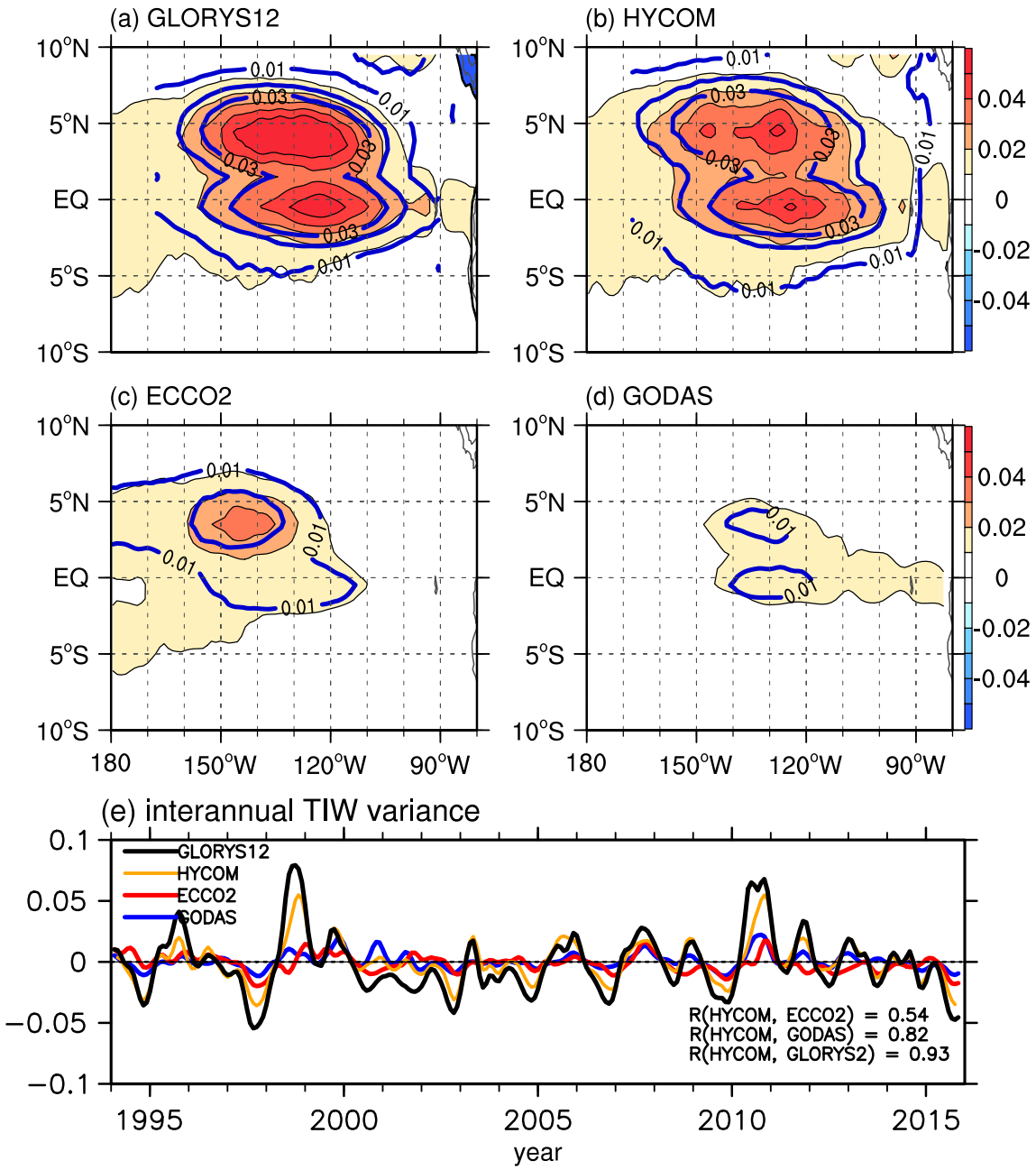

Fig. 10 **a–d** Mean state of TIWs variances calculated from the traditional 10–60-day band-pass filtered meridional velocity anomalies (v') within the mixed layer (shadings, units: m^2s^{-2}) and TIWs amplitudes derived from new method described in Sect. 2.2 (contours, units: m^2s^{-2}) for GLORYS12, HYCOM, ECCO2 and GODAS datasets, respectively; **e** Interannual part of three-month running mean and area-averaged (0–6°N, 110–150°W) monthly TIWs variance time series from the four datasets. Correlations between every two datasets are included in the bottom right corner

Table 3 Parameters values of K_0, K_1 and K_2 in the parameterization scheme of the four datasets with different horizontal resolutions

Datasets	K_0 (10^6)	K_1 (10^6)	K_2 (10^6)
GLORYS12(1/12°×1/12°)	− 0.55	− 0.20	0.10
HYCOM(1/12°×1/12°)	− 0.54	− 0.20	0.10
ECCO2(1/4°×1/4°)	− 0.36	0.10	0.002
GODAS(1°×1/3°)	− 0.40	− 0.005	0.01

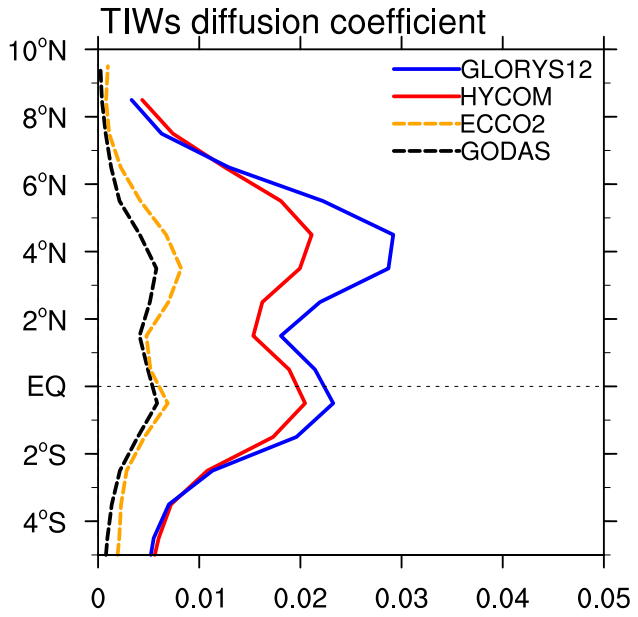

Fig. 11 Meridional profiles of TIWs mean diffusion coefficients K (units: m^2/s) in the parameterization scheme for GLORYS12 (red line), HYCOM (blue line), ECCO2 (black line) and GODAS (orange line) datasets, respectively

resolution based on four different oceanic reanalysis datasets (GLORYS12, HYCOM, ECCO2 and GODAS).

First, we display the representation of TIWs variances (v'^2) in these four datasets. TIWs activity exhibits similar double-peak patterns in the HYCOM and GLORYS12 characterized by high horizontal resolutions (Fig. 10a and b). In contrast, TIWs are seriously underestimated in the reanalysis datasets with low horizontal resolutions (GODAS and ECCO2) (Fig. 10c, d). The equatorial current system has been shown to be poorly reproduced in these two coarse datasets, which could lead to biases in the performance of TIWs simulation (Huang et al. 2010; Wang et al. 2020). The inter-comparison of interannual TIWs variance in Fig. 10e show that TIWs variance is nearly 50% larger in the high than low resolution datasets, despite high correlations between the different time series. Consistent with the TIW variances, the magnitudes of meridional heat transport are also much weaker in GODAS and ECCO2 compared to the estimates from HYCOM and GLORYS12 (not shown). It suggests that increasing the resolution of models help to simulate more realistically the TIWs activity and therefore its thermal feedback on the ENSO variability (Jochum et al. 2005; Imada and Kimoto 2012; Graham 2014; Wengel et al. 2021).

Since the four datasets are characterized by contrasted representations of TIWs features, different key parameters are derived when we develop the corresponding parameterization schemes using the multiple linear regression method. The estimated key parameters (K_0,K_1 and K_2) from the four datasets are shown in Table 3. The parameters from the GLORYS12 and HYCOM datasets are almost the same, identical to the estimates from one-dimensional formulation in our earlier studies (Xue et al. 2020; Boucharel and Jin 2020). However, the magnitudes of these parameters in the GODAS and ECCO2 datasets are much smaller, leading to the smaller eddy diffusion coefficients K (Fig. 11). The spatial resolutions of datasets affect their performances in simulating the spatiotemporal variability of TIWs amplitude and associated heat exchange rate in the EEP.

Correspondingly, the TIWs-induced heat fluxes exhibit high sensitivity to the spatial resolutions with contrasted performances (Fig. 12a–d). Regardless, the self-adaptable parameterization scheme can reproduce the realistic TIWs-induced heat flux for each dataset. As shown in Fig. 12e–h, the interannual time series of TIWs-induced heat fluxes estimated from our scheme and traditional method are all highly correlated, and our scheme successfully captures the modulations of ENSO and associated nonlinearity on TIWs activity. Given the climate mean TIWs variance (i.e., TIWs amplitude) based on high-resolution reanalysis or observation, our parameterization scheme can be used to correct the biases of TIWs-induced NDH in current climate models by employing their own ENSO low-frequency information.

6 Conclusions and discussion

In this study, we propose a parameterization scheme of the interannual TIWs-induced heat transport feedback on ENSO in terms of the slowly-varying meridional temperature gradient, a key factor governing the baroclinic energy conversion from the EEP mean state to TIWs mesoscale activity. Following the stochastic linear model of TIWs introduced by Boucharel and Jin (2020), the analytical solution of one-dimensional (temporal) TIWs-induced heat flux and NDH is extended to three-dimensions, describing the spatial and temporal features of TIWs. The parameterization scheme of TIWs-induced heat flux can be delineated by the direct linear ENSO effect, ENSO-cold tongue annual cycle combination

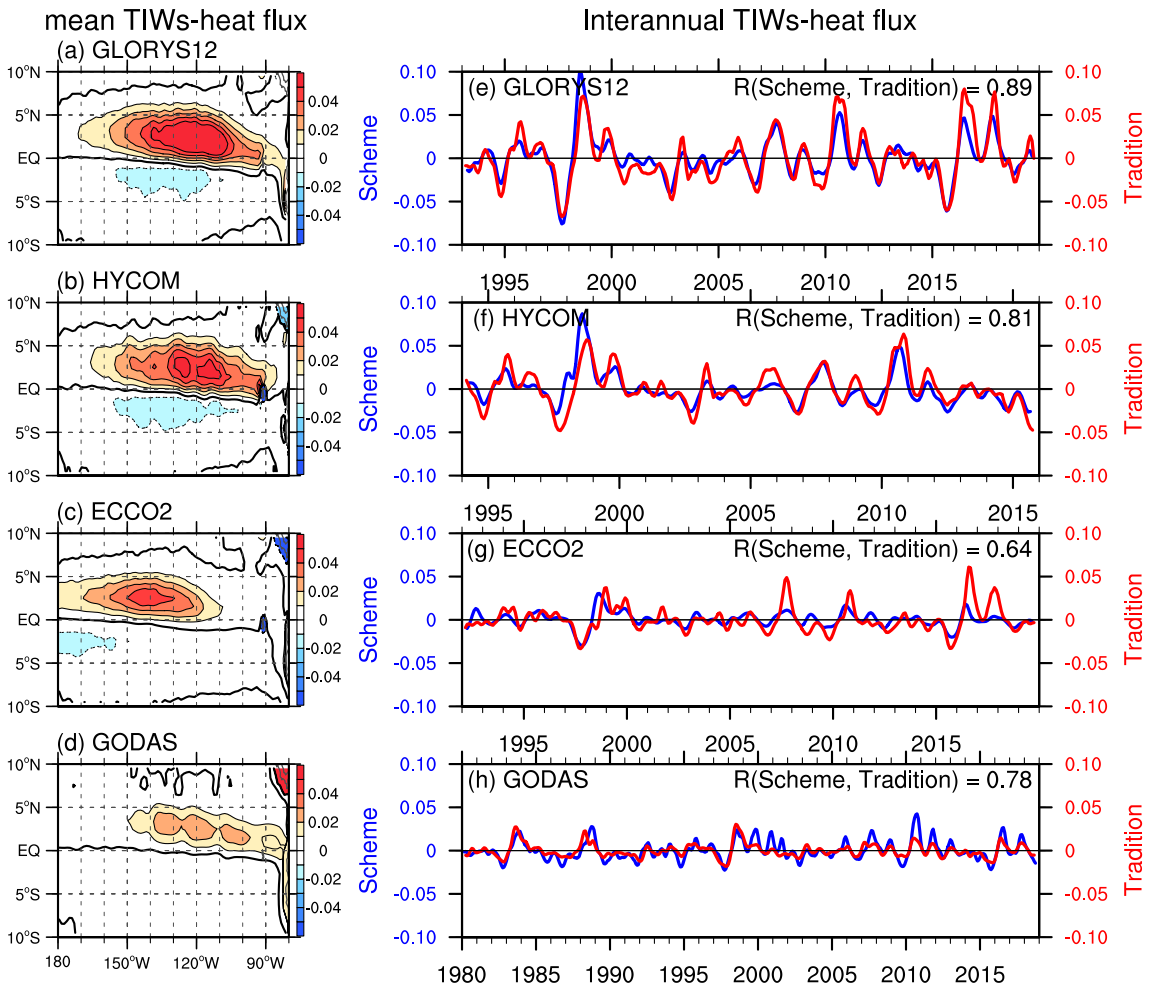

Fig. 12 **a–d** Comparisons of mean states of TIWs-induced heat flux within mixed layer (0–50 m) from GLORYS12, HYCOM, ECCO2, and GODAS datasets, respectively; **e–h** Interannual parts of the three-month running mean and area-averaged (0–6°N, 110–150°W) time series of the observed (red line) and parameterized (blue line) TIWs-induced heat fluxes (units: m°Cs^{-1}) in the four datasets, respectively. Correlations are included in the top right corner of each panel

effect, and ENSO high-order nonlinearity effect. We further demonstrated that our parameterization scheme can well capture the TIWs-induced heat effect on ENSO via comparison with the traditional (band-pass filtering) method.

Four different global oceanic reanalysis datasets are also used to test the sensitivity of this scheme to the horizontal resolution. The newly-adopted parameterization scheme reproduces the TIWs-induced thermal feedback on ENSO more accurately in the high than low resolution oceanic datasets. Despite the sensitivity to the spatial resolutions, the proposed quantification achieves a high degree of effectiveness and universality in describing the TIWs-induced NDH. This framework could therefore be a useful tool for assessing the models' performance in representing the TIWs-induced heat transport and understanding the important role of TIWs-induced NDH feedback in ENSO complexity.

Due to the fact that the TIWs mean variance ($\overline{v'^2}$) and ENSO state in the parameterization scheme could not be known a prior (i.e., calculated online), we should note that this scheme could not be included in ocean climate models to represent TIWs-induced eddy effects on the large-scale mean flow and slow climate variability in non-eddy resolving climate models. However, this formalism could still easily be implemented in middle hierarchical ENSO models such as the Zebiak and Cane model (ZC; Cane et al. 1986; Zebiak and Cane 1987) since the ENSO is a state variable in the ZC model and $\overline{v'^2}$ could be inferred from observations and imposed as a parameter. We are currently in the process of incorporating the scheme into the ZC model to investigate the TIWs' impact on ENSO and potentially improve performance in ENSO simulation and prediction. We will particularly examine the TIWs-induced NDH feedback on

the spatial structure of ENSO amplitude and asymmetry. Beyond the expected insights gained into ENSO's nonlinear dynamics, we believe such applications could pave the way for a long overdue revisit of the Gent and McWilliams parameterization (Gent and Mcwilliams 1990; Gent et al. 1995). In particular, it was originally developed to improve the representation by non-eddy resolving general circulation models of the effects of mesoscale activity on mid- and high-latitude flows that are characterized by very different Rossby radii and eddy diffusivity coefficients than those of equatorial regions where TIWs are present.

Acknowledgements This work was supported by the National Nature Science Foundation of China (42088101, 42125501).

Author contributions All authors contributed to the study completion. Material preparation, data collection and analysis were performed by AX. F-FJ and AX mainly conceived and designed the analysis. WZ and JB mainly reviewed and revised the manuscript. J-SK gave constructive suggestions and comments on the manuscript. All authors read and approved the final manuscript.

Funding Wenjun Zhang was supported by the National Nature Science Foundation of China (42088101, 42125501). Fei-Fei Jin was supported by U.S. National Science Foundation (AGS-1813611) and Department of Energy (DE-SC0005110). Julien Boucharel is funded by the French Agence Nationale de la Recherche project MOPGA "Trocodyn" (ANR-17-MPGA-0018) and the Région Occitanie. Jong-Seong Kug was supported by the National Research Foundation of Korea (NRF) grant funded by the Korean government (NRF-2022R1A3B1077622, NRF-2018R1A5A1024958).

Data availability All the datasets generated and/or analysed during the current study are available from the following resources: GODAS data is available at http://apdrc.soest.hawaii.edu/dods/public_data/Reanalysis_Data/GODAS/pentad; ECCO2 is downloaded from http://apdrc.soest.hawaii.edu/dods/public_data/ECCO/ECCO2/cube92; HYCOM datasets is from http://apdrc.soest.hawaii.edu/datadoc/hycom.php; GLORYS12 dataset is available at https://resources.marine.copernicus.eu/product-download/GLOBAL_MULTIYEAR_PHY_001_030.

Declarations

Conflict of interest The authors have no relevant financial or non-financial interests to disclose.

Ethical approval Not applicable.

Consent to participate Not applicable.

Consent for publication Not applicable.

References

An S-I (2008) Interannual variations of the tropical ocean instability wave and ENSO. J Clim 21:3680–3686. https://doi.org/10.1175/2008JCLI1701.1

Baturin NG, Niiler PP (1997) Effects of instability waves in the mixed layer of the equatorial Pacific. J Geophys Res Oceans 102:27771–27793. https://doi.org/10.1029/97JC02455

Behringer D, Xue Y (2004) Evaluation of the global ocean data assimilation system at NCEP: The Pacifc Ocean. In: Proc. Eighth Symp. on Integrated Observing and Assimilation Systems for Atmosphere, Oceans, and Land Surface, AMS 84th Annual Meeting, Washington State Convention and Trade Center, Seattle, Washington, 11–15 January 2004. [http://ams.confex.com/ams/pdfpapers/70720.pdf]

Boucharel J, Jin F-F (2020) A simple theory for the modulation of tropical instability waves by ENSO and the annual cycle. Tellus Dyn Meteorol Oceanogr 72:1700087. https://doi.org/10.1080/16000870.2019.1700087

Bryan K, Dukowicz JK, Smith RD (1999) On the mixing coefficient in the parameterization of bolus velocity. J Phys Oceanogr 29:2442–2456. https://doi.org/10.1175/1520-0485(1999)029%3c2442:OTMCIT%3e2.0.CO;2

Bryden HL, Brady EC (1989) Eddy momentum and heat fluxes and their effects on the circulation of the equatorial Pacific Ocean. J Mar Res 47:55–79. https://doi.org/10.1357/002224089785076389

Cane MA, Zebiak SE, Dolan SC (1986) Experimental forecasts of El Niño. Nature 321:827–832. https://doi.org/10.1038/321827a0

Chassignet EP, Hurlburt HE, Smedstad OM et al (2007) The HYCOM (HYbrid Coordinate Ocean Model) data assimilative system. J Mar Syst 65:60–83. https://doi.org/10.1016/j.jmarsys.2005.09.016

Contreras RF (2002) Long-term observations of tropical instability waves. J Phys Oceanogr 32:2715–2722. https://doi.org/10.1175/1520-0485(2002)032%3c2715:LTOOTI%3e2.0.CO;2

Cox MD (1980) Generation and propagation of 30-day waves in a numerical model of the Pacific. J Phys Oceanogr 10:1168–1186. https://doi.org/10.1175/1520-0485(1980)010%3c1168:GAPODW%3e2.0.CO;2

Gent PR, Mcwilliams JC (1990) Isopycnal mixing in ocean circulation models. J Phys Oceanogr 20:150–155. https://doi.org/10.1175/1520-0485(1990)020%3c0150:IMIOCM%3e2.0.CO;2

Gent PR, Willebrand J, McDougall TJ, McWilliams JC (1995) Parameterizing Eddy-induced tracer transports in ocean circulation models. J Phys Oceanogr 25:463–474. https://doi.org/10.1175/1520-0485(1995)025%3c0463:PEITTI%3e2.0.CO;2

Graham T (2014) The importance of eddy permitting model resolution for simulation of the heat budget of tropical instability waves. Ocean Model 79:21–32. https://doi.org/10.1016/j.ocemod.2014.04.005

Hansen DV, Paul CA (1984) Genesis and effects of long waves in the equatorial Pacific. J Geophys Res 89:10431. https://doi.org/10.1029/JC089iC06p10431

Huang B, Xue Y, Zhang D et al (2010) The NCEP GODAS ocean analysis of the tropical Pacific mixed layer heat budget on seasonal to interannual time scales. J Clim 23:4901–4925. https://doi.org/10.1175/2010JCLI3373.1

Im S-H, An S-I, Lengaigne M, Noh Y (2012) Seasonality of tropical instability waves and its feedback to the seasonal cycle in the Tropical Eastern Pacific. Sci World J 2012:1–11. https://doi.org/10.1100/2012/612048

Imada Y, Kimoto M (2012) Parameterization of tropical instability waves and examination of their impact on ENSO characteristics. J Clim 25:4568–4581. https://doi.org/10.1175/JCLI-D-11-00233.1

Jin F-F (1997) An equatorial ocean recharge paradigm for ENSO. Part I: conceptual model. J Atmos Sci 54:811–829. https://doi.org/10.1175/1520-0469(1997)054%3c0811:AEORPF%3e2.0.CO;2

Jin F-F, An S-I, Timmermann A, Zhao J (2003) Strong El Niño events and nonlinear dynamical heating. Geophys Res Lett 30:1120. https://doi.org/10.1029/2002GL016356

Jin F-F, Kim ST, Bejarano L (2006) A coupled-stability index for ENSO. Geophys Res Lett 33:L23708. https://doi.org/10.1029/2006GL027221

Jochum M, Cronin MF, Kessler WS, Shea D (2007) Observed horizontal temperature advection by tropical instability waves. Geophys Res Lett 34:L09604. https://doi.org/10.1029/2007GL029416

Jochum M, Murtugudde R, Ferrari R, Malanotte-Rizzoli P (2005) The impact of horizontal resolution on the tropical heat budget in an Atlantic Ocean Model. J Clim 18:841–851. https://doi.org/10.1175/JCLI-3288.1

Kim ST, Jin F-F (2011) An ENSO stability analysis. Part I: results from a hybrid coupled model. Clim Dyn 36:1593–1607. https://doi.org/10.1007/s00382-010-0796-0

Legeckis R (1977) Long waves in the Eastern Equatorial Pacific Ocean: a view from a geostationary satellite. Science 197:1179–1181. https://doi.org/10.1126/science.197.4309.1179

Lellouche J-M, Eric G, Romain B-B et al (2021) The Copernicus global 1/12° oceanic and sea ice GLORYS12 reanalysis. Front Earth Sci 9:698876. https://doi.org/10.3389/feart.2021.698876

Lyman JM, Chelton DB, deSzoeke RA, Samelson RM (2005) Tropical instability waves as a resonance between equatorial Rossby waves. J Phys Oceanogr 35:232–254. https://doi.org/10.1175/JPO-2668.1

Maillard L, Boucharel J, Renault L (2022) Direct and rectified effects of tropical instability waves on the Eastern Tropical Pacific mean state in a regional ocean model. J Phys Oceanogr 52:1817–1834. https://doi.org/10.1175/JPO-D-21-0300.1

Masina S, Philander SGH, Bush ABG (1999) An analysis of tropical instability waves in a numerical model of the Pacific Ocean: 2. Generation and energetics of the waves. J Geophys Res 104:29637–29661. https://doi.org/10.1029/1999JC900226

Menemenlis D, Campin J-M, Heimbach P et al (2008) ECCO2: high resolution global ocean and sea ice data synthesis. Mercator Ocean Q Newsl 31:13–21

Menkes CER, Vialard JG, Kennan SC et al (2006) A Modeling study of the impact of tropical instability waves on the heat budget of the Eastern Equatorial Pacific. J Phys Oceanogr 36:847–865. https://doi.org/10.1175/JPO2904.1

North GR, Bell TL, Cahalan RF, Moeng FJ (1982) Sampling errors in the estimation of empirical orthogonal functions. Mon Weather Rev 110:699–706. https://doi.org/10.1175/1520-0493(1982)110%3c0699:SEITEO%3e2.0.CO;2

Philander SGH (1976) Instabilities of zonal equatorial currents. J Geophys Res 81:3725–3735. https://doi.org/10.1029/JC081i021p03725

Philander SGH (1978) Instabilities of zonal equatorial currents, 2. J Geophys Res Oceans 83:3679–3682. https://doi.org/10.1029/JC083iC07p03679

Pullen PE, Bernstein RL, Halpern D (1987) Equatorial long-wave characteristics determined from satellite sea surface temperature and in situ data. J Geophys Res Oceans 92:742–748. https://doi.org/10.1029/JC092iC01p00742

Qiao L, Weisberg RH (1995) Tropical instability wave kinematics: observations from the tropical instability wave experiment. J Geophys Res Oceans 100:8677–8693. https://doi.org/10.1029/95JC00305

Qiao L, Weisberg RH (1998) Tropical instability wave energetics: observations from the tropical instability wave experiment. J Phys Oceanogr 28:345–360. https://doi.org/10.1175/1520-0485(1998)028%3c0345:TIWEOF%3e2.0.CO;2

Saha S, Nadiga S, Thiaw C et al (2006) The NCEP climate forecast system. J Clim 19:3483–3517. https://doi.org/10.1175/JCLI3812.1

Shinoda T, Kiladis GN, Roundy PE (2009) Statistical representation of equatorial waves and tropical instability waves in the Pacific Ocean. Atmos Res 94:37–44. https://doi.org/10.1016/j.atmosres.2008.06.002

Stuecker MF, Jin F-F, Timmermann A (2015) El Niño–southern oscillation frequency cascade. Proc Natl Acad Sci 112:13490–13495. https://doi.org/10.1073/pnas.1508622112

Stuecker MF, Timmermann A, Jin F-F et al (2013) A combination mode of the annual cycle and the El Niño/Southern Oscillation. Nature Geosci 6:540–544. https://doi.org/10.1038/ngeo1826

Swenson MS, Hansen DV (1999) Tropical Pacific Ocean mixed layer heat budget: the pacific cold tongue. J Phys Oceanogr 29:69–81. https://doi.org/10.1175/1520-0485(1999)029%3c0069:TPOMLH%3e2.0.CO;2

Vialard J, Menkes C, Boulanger J-P et al (2001) A model study of oceanic mechanisms affecting equatorial Pacific Sea surface temperature during the 1997–98 El Niño. J Phys Oceanogr 31:1649–1675. https://doi.org/10.1175/1520-0485(2001)031%3c1649:AMSOOM%3e2.0.CO;2

Wang M, Xie S-P, Shen SSP, Du Y (2020) Rossby and Yanai modes of tropical instability waves in the equatorial Pacific Ocean and a diagnostic model for surface currents. J Phys Oceanogr 50:3009–3024. https://doi.org/10.1175/JPO-D-20-0063.1

Wang S, Jing Z, Wu L et al (2022) El Niño/Southern Oscillation inhibited by submesoscale ocean eddies. Nat Geosci 15:112–117. https://doi.org/10.1038/s41561-021-00890-2

Wang W, McPhaden MJ (1999) The surface-layer heat balance in the equatorial Pacific Ocean. Part I: mean seasonal cycle. J Phys Oceanogr 29:1812–1831. https://doi.org/10.1175/1520-0485(1999)029%3c1812:TSLHBI%3e2.0.CO;2

Weisberg RH, Weingartner TJ (1988) Instability waves in the equatorial Atlantic Ocean. J Phys Oceanogr 18:1641–1657. https://doi.org/10.1175/1520-0485(1988)018%3c1641:IWITEA%3e2.0.CO;2

Wengel C, Lee S-S, Stuecker MF et al (2021) Future high-resolution El Niño/Southern Oscillation dynamics. Nat Clim Change 11:758–765. https://doi.org/10.1038/s41558-021-01132-4

Wilson D, Leetmaa A (1988) Acoustic Doppler current profiling in the equatorial Pacific in 1984. J Geophys Res 93:13947. https://doi.org/10.1029/JC093iC11p13947

Wu Q, Bowman KP (2007) Interannual variations of tropical instability waves observed by the Tropical Rainfall Measuring Mission. Geophys Res Lett 34:L09701. https://doi.org/10.1029/2007GL029719

Xue A, Jin F-F, Zhang W et al (2020) Delineating the Seasonally Modulated Nonlinear Feedback Onto ENSO From Tropical Instability Waves. Geophys Res Lett 47:e2019GL085863. https://doi.org/10.1029/2019GL085863

Xue A, Zhang W, Boucharel J, Jin F-F (2021) Anomalous tropical instability wave activity hindered the development of the 2016/17 La Niña. J Clim 34:5583–5600. https://doi.org/10.1175/JCLI-D-20-0399.1

Yu J-Y, Liu WT (2003) A linear relationship between ENSO intensity and tropical instability wave activity in the eastern Pacific Ocean. Geophys Res Lett 30:1735. https://doi.org/10.1029/2003GL017176

Yu Z, McCreary JP, Proehl JA (1995) Meridional asymmetry and energetics of tropical instability waves. J Phys Oceanogr 25:2997–3007. https://doi.org/10.1175/1520-0485(1995)025%3c2997:MAAEOT%3e2.0.CO;2

Zebiak SE, Cane MA (1987) A model El Niño-southern oscillation. Mon Weather Rev 115:2262–2278. https://doi.org/10.1175/1520-0493(1987)115%3c2262:AMENO%3e2.0.CO;2